



Insights into highly efficient photodegradation of poly/perfluoroalkyl substances by In-MOF/BiOF heterojunctions: Built-in electric field and strong surface adsorption

Jingzhen Wang¹, Chun-Shuai Cao¹, Jingwen Wang, Yinqing Zhang, Lingyan Zhu^{*}

Key Laboratory of Pollution Processes and Environmental Criteria (Ministry of Education), Tianjin Key Laboratory of Environmental Remediation and Pollution Control, College of Environmental Science and Engineering, Nankai University, Tianjin 300350, China

ARTICLE INFO

Keywords:

Built-in electric field
In-MOF/BiOF heterojunction
Photodegradation
Poly/perfluoroalkyl substances

ABSTRACT

Poly/perfluoroalkyl substances (PFASs) are ubiquitous organic pollutants and the strong C—F bonds make them recalcitrant for degradation. In this study, novel In-MOF/BiOF heterojunctions at different doping ratios were synthesized, characterized and evaluated for the photocatalytic removal performance on Perfluorooctanonate (PFOA), perfluorooctane sulfonate (PFOS), hexafluoropropylene oxide trimer acid (HFPO-TA) and 6:2 chlorinated polyfluorinated ether sulfonate (6:2 Cl-PFESA). 20% In-MOF/BiOF exhibited effective and complete degradation of PFOA (15 mg/L) under illumination. The reaction rate constants decreased in the order of PFOS > 6:2 Cl-PFESA > PFOA > HFPO-TA. The density functional theory calculation revealed that the reaction rate constant positively correlated with adsorption energies of the PFASs on the catalyst. Additionally, the generation of built-in electric field at the In-MOF and BiOF interfaces enhanced the efficient separation of photogenerated carriers, thus intrinsically facilitated the catalytic performance. The study sheds light on the construction of built-in electric field to improve photocatalytic performance.

1. Introduction

Poly/perfluoroalkyl substances (PFASs), due to their special hydrophobic and oleophobic properties as well as high stability, have been widely applied in various industrial products including surfactants, textile coatings, food contact materials, pesticide formulas and fire-fighting foam [1]. PFASs become ubiquitous and global contaminants, particularly in aquatic environments, such as municipal sewage, surface water and even drinking water [2,3]. Their strong persistence and potential adverse effects to organisms and human beings have attracted great concerns over the pollution control of PFASs [4,5]. Stringent regulations have been executed to limit the production and usage of perfluorooctanonate (PFOA), perfluorooctane sulfonate (PFOS), and their salts [6,7]. Many emerging PFASs, for example, 6:2 chlorinated polyfluorinated ether sulfonate (6:2 Cl-PFESA) and hexafluoropropylene oxide trimer acid (HFPO-TA), were developed to replace PFOS or PFOA [8,9]. It is worth mentioning that HFPO-TA displays stronger hepatotoxicity and higher bioaccumulation potential than PFOA [10]. Recent studies indicated that HFPO-TA and 6:2 Cl-PFESA, as substituents for

PFOA and PFOS, were frequently detected in water samples of the world [11,12], with concentrations similar or even higher than those of PFOA/PFOS in some places [13,14]. It is extremely difficult to decompose PFASs by traditional wastewater treatment technologies, because of the strong electronegativity of F atoms and the remarkably high C—F bond energy (533 kJ mol^{-1}) [15]. A number of photocatalysts have been developed to degrade PFOA efficiently, but few of them performed well in PFOS degradation, suggesting that it is even more difficult to degrade PFOS than PFOA, and the chemical structures of PFASs greatly impact the removal performance [16–19]. The emerging PFASs are different from the legacy ones in structures, and there are limited studies on the pollution control of these emerging PFASs. Since legacy and emerging PFASs are always co-present in water, it is urgent to seek promising photocatalysts to remove them simultaneously.

Over the past decades, environmentally friendly and economical photocatalysts have been successfully fabricated for decomposing various toxic substances [20–23]. However, fast electron-hole recombination and low utilization efficiency of light energy limit the applications of these single component photocatalysts. Therefore, various

^{*} Corresponding author.

E-mail address: zhuly@nankai.edu.cn (L. Zhu).

¹ These authors contributed equally to this work.

strategies have been developed to break through this bottleneck and inspire the improvement of photocatalytic activity, mainly including facet engineering [24], crystal morphology [25], metal loading [26], ion doping [27], and construction of heterojunctions [28]. In recent years, construction of built-in electric field has been proven to be a powerful solution to achieve maximal carrier separation. The transfer of photo-generated electrons and holes in reverse direction motivated by built-in electric field drastically expedite the separation of the pairs [29,30]. Among these compounds, bismuth-based oxyhalides (BiOX, X = F, Cl, Br, I) have been widely investigated due to their favorable energy gaps, remarkable chemical stability, unique layered structure and highly satisfactory photocatalytic performance [31,32]. Particularly, the atomic arrangements in BiOX are composed of $[\text{Bi}_2\text{O}_2]^{2+}$ slabs interweaved with double $[\text{X}_2]^{2-}$ layers to form self-assembling internal electrostatic field, which is beneficial to the separation and migration of the photoinduced e^-h^+ pairs and enables them to exhibit satisfactory photocatalytic activities [33]. Due to the presence of high energy C—F bonds in PFASs, a stronger redox capacity is required to decompose them. Bismuth oxyfluoride (BiOF) possesses a band gap of 3.5 eV, thus it is sensitive to light in UV region and equips with high redox capacity [34]. Our previous study demonstrated that BiOF with highly exposed (101) facets exhibited outstanding degradation and mineralization efficiency to PFOA [35]. But its capacity to degrade PFOS and the emerging PFASs should be further examined and improved.

In recent years, photoactive Metal-Organic Frameworks (MOFs) that consist of metal clusters/ions and organic linkers have attracted much interest in photocatalytic aspects, due to their high specific surface area, sufficient exposed active sites and functional tunability [36]. The metallic clusters or ions mainly contain di/trivalent cations of 3d transition metals (e.g., Fe, Zn, Ni, Co, In, Ti) and 3p metals [37]. Upon light irradiation, the outer orbitals of organic ligands in the photoactive MOFs contribute to the valence band, while the empty orbitals of the metal center contribute to the conduction band [38]. Nevertheless, the single MOFs-based photocatalysts usually do not work very well to degrade organic contaminants [39]. As MOFs are doped with other photocatalysts, they not only crucially modify the electronic structures of conventional photocatalysts, but also play the role of donor or acceptor to improve the hole-electron separation. For example, Yu et al. fabricated a macroporous Si (MPSi)/Gr heterojunction to convert solar light to chemical energy [40]. Gong et al. constructed g-C₃N₄/MIL-101(Fe) composites to improve the catalytic efficiency for degradation of bisphenol A under visible light irradiation [41]. A UiO-66/CdS hybrid exhibited high-efficient photocatalytic H₂ production [42]. Indium is a good candidate of 3d transition metals, and the structure of In-MOF has been reported previously [43], but its application on degradation of persistent organic pollutants has never been deeply studied.

In this study, a series of In-MOF/BiOF composites with different doping ratios were constructed by a facile solvothermal method, and characterized by a variety of analytical techniques. Taking the degradation of PFOA in water as a model reaction, the reaction conditions and doping ratio were optimized by evaluating the photocatalytic performance. The electron paramagnetic resonance (EPR) spectroscopy measurement and reactive species capture experiments were conducted to unveil the mechanisms accounting for PFASs degradation. Density functional theory (DFT) analysis was utilized to elucidate the intrinsic mechanisms for the improvement of photocatalytic activity.

2. Materials and methods

2.1. Chemicals and reagents

InCl₃ was purchased from Hengshan Chemical Co., Ltd., Tianjin, China. 1,4-Benzenedicarboxylic acid (BDC) was purchased from Heowns Biochemical Technology Co., Ltd., Tianjin, China. N,N'-dimethyl formamide (DMF) were obtained by Concord Technology Co., Ltd., Tianjin, China. Bi(NO₃)₃·5H₂O was provided by McLean Biochemical

Technology Co., Ltd, Shanghai, China. Ethylene glycol was afforded by Tianjin Balens Biotechnology Co. Ltd., China. The t-butanol, ammonium oxalate (AO), NaF, KBrO₃, Na₂SO₄, ammonium acetate and benzoquinone (BQ) were provided by Guangfu Technology Development Co. Ltd., Tianjin, China. PFOS, PFOA and 6:2 Cl-PFESAs with > 99% purity were supplied by Wellington Laboratories (Guelph, Canada), while HFPO-TA was purchased from Fluorochem (Old Glossop, UK). All the solutions were prepared with MilliQ ultrapure water. MilliQ ultrapure water and high-performance liquid chromatography grade methanol (Dikma Chemical) were used as mobile phase. All other reagents were analytical grade and used directly without further purification.

2.2. Preparation of photocatalysts

2.2.1. Preparation of In-MOF

In-MOF was prepared using a hydrothermal method: a mixture of InCl₃ (0.9 mmol, 0.1990 g), BDC (0.8 mmol, 0.1328 g), H₂O (1 mL) and DMF (4 mL) was sealed in a 25 mL Teflon-lined stainless vessel, and the vessel was heated to 140 °C during 3 h in an oven, kept at 140 °C for 48 h and cooled down to room temperature at a rate of 4.58 °C/h. Colorless and rod like crystals were obtained, which were filtered and washed with DMF for three times. The obtained solids were activated with chromatographic grade CH₂Cl₂ for 5 d, and dried at 80 °C for 24 h.

2.2.2. Preparation of In-MOF/BiOF

In a typical procedure, 0.97 g of Bi(NO₃)₃·5H₂O was dissolved in 20 mL of ethylene glycol to form transparent solution A, and 0.08 g of NaF was dissolved in 20 mL of H₂O to form transparent solution B. After ultrasonication for 30 min, solution B was drop-wisely added into solution A under constant stirring. A certain amount (0.043, 0.086, 0.129, 0.172 g) of In-MOF was added into the mixed solution, and ultrasonicated for 10 min. The resulted solution was transferred to a 100 mL Teflon-lined stainless vessel, which was sealed and heated in an oven at 160 °C for 24 h. Subsequently, the solids were collected by centrifugation after cooling down to room temperature naturally, and washed with deionized water and ethanol for several times. Afterward, the greyish precipitates were dried at 80 °C for 24 h to obtain the as-prepared 10%, 20%, 30% and 40% In-MOF/BiOF composites. For comparison, pure BiOF was prepared following the same procedures without addition of In-MOF.

2.3. Characterization of the photocatalysts

The crystal structures of the prepared materials were analyzed by an X-ray diffractometer (XRD, Ulitima IV) by Cu-K α radiation under 40 kV and 100 mA with 10°/min from 5° to 80°. A field emission scanning electron microscopy (FESEM, JSM-7800F, Japan) was applied to observe the morphology and elemental compositions of the photocatalysts. The specific surface area was determined by ASAP 2020 Brunauer-Emmett-Teller (BET) method (BET, Micromeritics, America) and pore size distribution was analyzed on the sorption/desorption isotherms of N₂ adopting the Barrett-Joyner-Halenda (BJH) equation by surface area and porosimetry analyzer (ASAP 2460, Micromeritics, 46 USA). Thermogravimetric analysis (TGA) was performed by Simultaneous Thermal Analyzer (TGA/DSC1, Mettler-Toledo, Zurich). The concentration of In in the photocatalysts was determined by inductively coupled plasma mass spectrometry (ICP-MS, Elan DRC-e, PerkinElmer, USA). Then, the actual contents of In-MOF in 10%, 20%, 30% and 40% In-MOF/BiOF composite materials were calculated to be 9.1%, 17.1%, 21.7% and 31.0%, respectively. The chemical states and elemental compositions were measured by X-ray Photoelectron Spectroscopy (XPS) (250xi, Thermo ESCALAB). A total organic carbon analyzer (TOC Multi N/C3100, Analytic Jena, Germany) was used to measure the content of total organic carbon of the reaction solutions.

2.4. Photoelectrochemical measurement

The optical absorption property of In-MOF/BiOF composites was measured by a Hitachi U-3900H UV–vis diffuse reflectance spectrometer (UV-DRS, U-3900H, Techcomp, China) with BaSO₄ as reference during the test, and the spectral range was 200–800 nm. The transfer and recombination of the photogenerated electron hole pairs of the composites were performed and assessed by F-4600 photoluminescence spectroscopy (PL, Hitachi, Japan). Photoelectrochemical signals of the samples were obtained using an electrochemical workstation (760E, Shanghai Chenhua, China) with conventional three-electrodes (ITO/photocatalyst electrode with area of 1 cm² as the working electrode, platinum wire as counter electrode and Ag/AgCl electrode as reference electrode, respectively). The single-compartment quartz cell (100 mL) filled with 50 mL of 0.2 M Na₂SO₄ electrolyte, which was irradiated by the light source (PLS-SXE 300, Perfectlight Co., Ltd., Beijing, China) to afford continuously adjustable wavelengths. The transient response of the photocurrent was tested at 0.0 V, and controlled by regular switching lamp as light on and off at certain intervals. The electron paramagnetic resonance (EPR) spectroscopy measurement was performed on a spectrometer (JES FA300, Japan) under light at room temperature.

2.5. Degradation experiments

The photocatalytic degradation of the PFASs were carried out in an XPA-7 photochemical reactor (Xujiang Electromechanical plant, Nanjing, China) equipped with 12 quartz tubes (50 mL) under simulated UV-light irradiation to evaluate the photocatalytic properties. In the reaction, a certain amount of catalyst was added into the quartz tubes, then added with 40 mL of the individual PFASs (each at 15 mg/L), and the reaction tubes were maintained at room temperature by circulating water. Before illumination, the mixture was stirred for 1 h to establish adsorption equilibrium of PFASs on the catalysts, and the light irradiation was provided by a 500 W Hg lamp (the spectrum is shown in Fig. S1) with the stirring still going on. During the 180 min of reaction process, an aliquot of the reaction solution (1 mL) was sampled from the reaction system at predetermined intervals and filtered through 0.22 µm needle filter. All the samples were put into the sampling vials. To evaluate the stability of the catalysts, the photocatalyst after each cycle of reaction was recovered and washed sequentially with ethanol and deionized water, and then dried at 80 °C for 12 h. The recycled photocatalyst was then used for another degradation test following the above procedures. The details of PFASs analysis are shown in the Supporting Information (SI).

2.6. Theoretical analyses and computational modeling

All the first-principle spin-polarized calculations were performed using the Vienna ab initio simulation package [44,45]. The ion-electron interactions were described by the projector augmented wave method, and the generalized gradient approximation [46] in the Perdew–Burke–Ernzerhof form [47] and a cutoff energy of 500 eV for plane-wave basis set was adopted. The convergence threshold was 10^{−5} eV, and 5 × 10^{−3} eV/Å for energy and force, respectively, during the structure relaxation. The weak interaction was described by DFT+D3 method using empirical correction in Grimme's scheme [48]. The Monkhorst–Pack k-point mesh was set to 2 × 2 × 1. A vacuum space exceeds 15 Å was employed to avoid the interaction between two periodic units. For the BiOF material, the (001) surface was used during the calculation. The calculation methods of the adsorption of PFASs on the photocatalysts are described in the Supporting Information (SI).

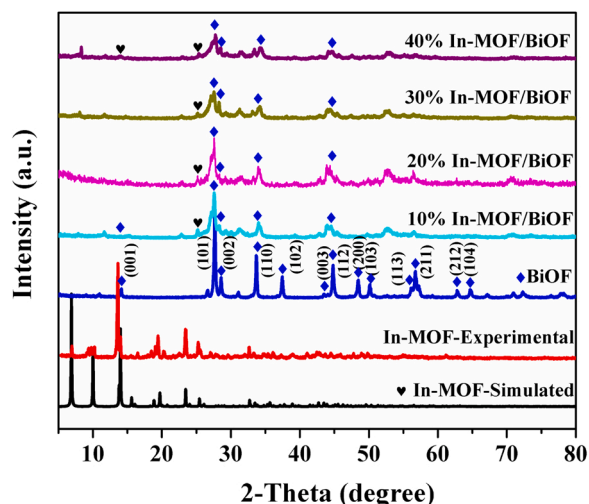


Fig. 1. The XRD patterns of simulated In-MOF, prepared In-MOF, BiOF, 10% In-MOF/BiOF, 20% In-MOF/BiOF, 30% In-MOF/BiOF and 40% In-MOF/BiOF.

3. Results and discussion

3.1. Characterization of the as-prepared photocatalysts

In this study, colorless and rod like crystals of In-MOF were synthesized, and the single-crystal X-ray analysis indicated that the In-MOF was in a trigonal crystal system with space group *P*3₂21 (Table S1). Each asymmetric unit consisted of one crystallographically independent In (III) ion and one BDC^{2−} anion in In-MOF. The coordination environment of In(III) ion was furnished by eight O atoms from four BDC ligands, and the BDC^{2−} anion was coordinated with two In(III) ions (Fig. S2a). The In centers and BDC ligands constructed a 3D framework equipped with a 1D pore channel with the diameter of about 14.7 Å (Fig. S2b, c). From the topological view, each In(III) ion linked with four ligands and was considered as a 4-connected node. Therefore, the 2-fold parallel interpenetrating networks can be designated as a uninodal 4-c net with qtz topology and Schläfli symbol for the net as {6⁴8²} (Fig. S2d). The XRD patterns of the simulated In-MOF, the as-prepared In-MOF, BiOF, 10–40% In-MOF/BiOF composites are shown in Fig. 1. The XRD patterns of all the In-MOFs are almost identical to the simulated one, manifesting that In-MOF was in pure phase. The XRD diffraction peaks of the prepared BiOF are well indexed to the crystal planes of the standard (JCPDS: No. 86–1648), proving that pure BiOF was synthesized successfully. As for the In-MOF/BiOF composites with different doping ratios, the main characteristic peaks of BiOF were distinct, but those of In-MOF were negligible, indicating a small amount of In-MOF was doped in the structure of BiOF. With the increase of doped amount of In-MOF, the relative intensities of some characteristic peaks decreased compared with those of pure BiOF, indicating that the crystallinity of the composites was influenced by the introduction of In-MOF.

Fig. S3 depicts the SEM images of In-MOF, BiOF, and their composites. The pure In-MOF was assembled in nanorods with the size of 50–150 µm, while BiOF was in flower-like microspheres assembled by nanosheets of 100–200 nm. As In-MOF was doped in BiOF, the nanorods of In-MOF were dispersed into the loose microspheres of BiOF, which was conducive for the increase of pore volume and specific surface area. The elemental mappings of 20% In-MOF/BiOF proved that In-MOF and BiOF were evenly distributed in the composites, allowing sufficient interface contact between them (Fig. 2a, c–f, Scheme S1), and then fast transport of charge carriers during the reaction. The EDS spectra further proved that the composites were mainly composed of BiOF and a small amount of In-MOF (Fig. 2b).

The N₂ adsorption/desorption isotherms of BiOF, In-MOF and 20% In-MOF/BiOF are displayed in Fig. S4a, and their isotherms were all

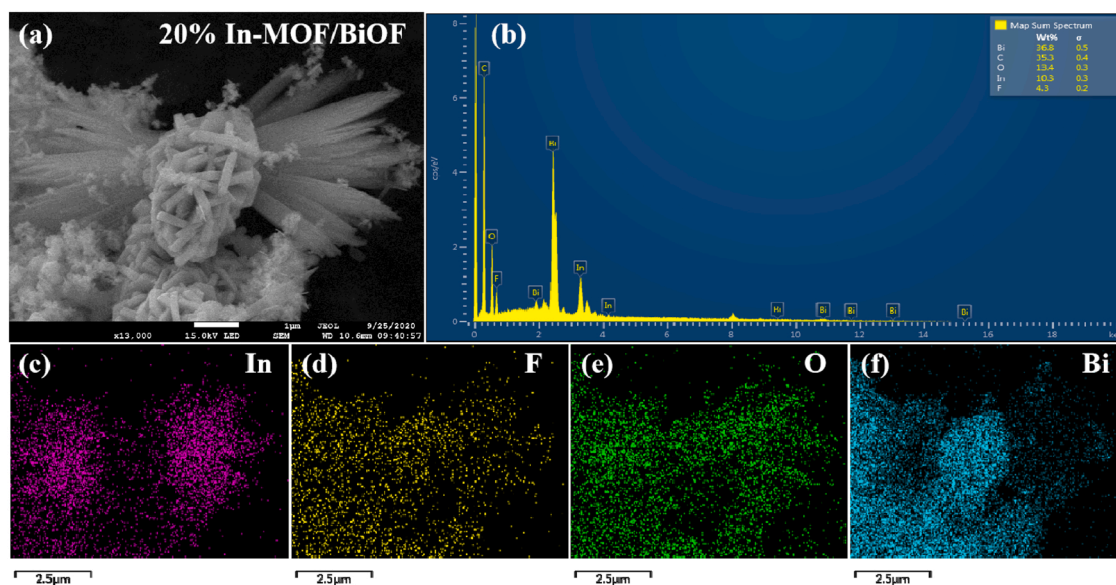


Fig. 2. The SEM image (a), the EDS spectrum of elements (b) and elemental mappings (c–f) of 20% In-MOF/BiOF photocatalysts.

characteristic of type IV with a hysteresis loop. Compared with BiOF, the adsorption of N_2 in 20% In-MOF/BiOF composite increased due to the doping of In-MOF, fortifying that the pore volume and specific surface area were vastly improved. Pore-size distribution curves also exhibited that the pores of 20% In-MOF/BiOF were mainly distributed in the range of 2–20 and 26–35 nm, while the pores of pure BiOF were much smaller (8–11 nm) (Fig. S4b). This suggested that the introduction of In-MOF effectively enlarged the pores of the composites. Thus, the composites were featured by mesoporous structure and the pores were larger than those of pure BiOF. The BET surface area, pore volume and pore diameter of BiOF, In-MOF and 20% In-MOF/BiOF are listed in Table S2.

The TGA analysis showed that In-MOF was stable below 420 °C, and the TGA curve of 20% In-MOF/BiOF indicated that it had very good thermal stability, which was almost in accord with that of BiOF (Fig. S5). The XPS survey was employed to investigate the element compositions. As presented in Fig. S6, the XPS spectrum indicated that there were only C, O, F, Bi and In elements in the composites. In both In-MOF and 20% In-MOF/BiOF, the two characteristic peaks of C 1s positioned at 284.8 eV and 288.8 eV, corresponding to the sp^2 C=C and O-C=O groups [49,50]. As for O 1s spectrum, there were two characteristic peaks at 531.7 eV and 532.4 eV, which were assigned to In–O and C=O

bonds of In-MOF, respectively. Moreover, the O 1s spectrum of BiOF was divided into two characteristic peaks with binding energies at 530.1 eV and 531.3 eV, corresponding to the Bi–O bonds and H_2O/OH^- adsorbed on BiOF, respectively [51,52]. Meanwhile, the peaks of In–O (531.7 eV), C=O (532.4 eV) and Bi–O bonds (530.1 eV) were clearly observed in the O 1s spectrum of 20% In-MOF/BiOF. The slight peak shift of the C=O bond was attributed to the chemical interactions between In-MOF and BiOF. However, the peak of H_2O/OH^- at 531.3 eV in the O 1s spectrum of 20% In-MOF/BiOF was overlapped by that of In–O bond at 531.7 eV. In addition, the characteristic peak of F 1s was observed at 683.7 eV in the spectrum of both BiOF and 20% In-MOF/BiOF. The peaks of Bi 4 $f_{7/2}$ (at 159.2 eV) and Bi 4 $f_{5/2}$ (at 164.5 eV) were assigned to Bi (III). The energy gap between the binding energies of In 3 $d_{5/2}$ (at 445 eV) and In 3 $d_{3/2}$ (at 452.6 eV) was approximate 7.6 eV in 20% In-MOF/BiOF, which was consistent with those in In (III) compounds [53,54].

3.2. Photocatalytic performances of the as prepared photocatalysts

The photocatalytic performances of the as-prepared In-MOF, BiOF, 10%–40% In-MOF/BiOF composites were evaluated by degrading PFOA

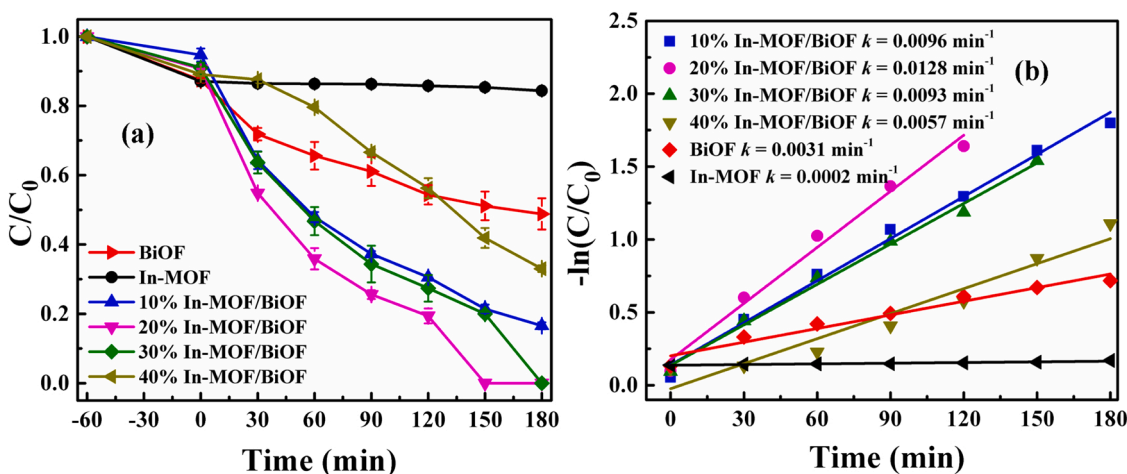


Fig. 3. (a) Adsorption and degradation of PFOA by different photocatalysts under light irradiation; (b) The pseudo-first-order fitting of PFOA by the as-prepared different catalysts.

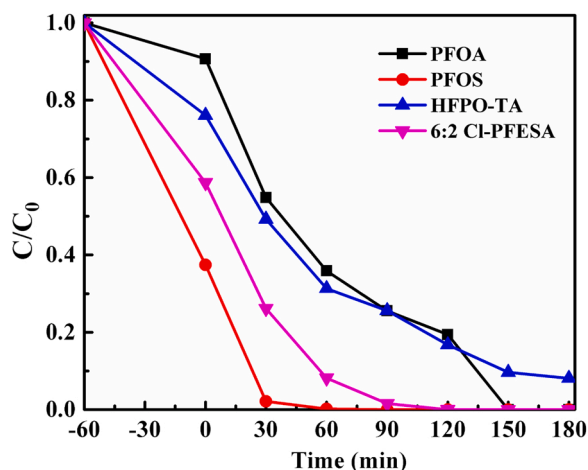


Fig. 4. Adsorption and degradation of PFOA, PFOS, HFPO-TA and 6:2 Cl-PFESA by 20% In-MOF/BiOF.

(15 mg/L) under light irradiation for 180 min Fig. 3a shows that only 16% of PFOA was adsorbed on pure In-MOF without obvious degradation, and only 51% of PFOA was decomposed by pure BiOF during 180 min. However, PFOA was completely degraded by the 20% In-MOF/BiOF and 30% In-MOF/BiOF within 150 and 180 min, respectively. In addition, 10% In-MOF/BiOF and 40% In-MOF/BiOF could also remove about 83% and 67% PFOA within 180 min irradiation, respectively. Compared with the photochemical degradation efficiency of PFOA reported previously (Table S3), the photocatalyst provided in this study shows excellent photocatalytic performance, which effectively shortens the time required for complete degradation of PFOA.

The reaction rate constants (k_{obs} , min^{-1}) were calculated based on the pseudo-first-order kinetics equation: $-\ln(C_t/C_0) = k_{\text{obs}} \cdot t$, where C_t and C_0 mean the concentration of PFOA at reaction time t and 0 min, respectively. As shown in Fig. 3b, the k_{obs} of In-MOF, BiOF, 10%–40% In-MOF/BiOF was 0.0002, 0.0031, 0.0096, 0.0128, 0.0093, 0.0057 min^{-1} , respectively. The k_{obs} of PFOA degradation catalyzed by 20% In-MOF/BiOF was 4.13 times of the pure BiOF. The results testified

that the photocatalytic activity of BiOF was obviously improved after doping with In-MOF. Thus, 20% In-MOF/BiOF was selected as the main catalyst in the following experiments, and the optimized reaction conditions were determined as 0.5 g/L of 20% In-MOF/BiOF, 40 mL of PFOA (15 mg/L) under 180 min irradiation (Fig. S7). The mineralization of organic pollutants is usually used for analyzing the degradation efficiency of catalysts. Fig. S8 shows that TOC of the reaction solution decreased by 37.7% and the final defluorination efficiency was about 34% after 180 min light irradiation. The concentration of the released F gradually increased with the extension of reaction time, proving that C–F bonds were successfully destroyed.

As a heterogeneous catalyst, the reusability of photocatalyst is an indispensable parameter for further practical application. The results in Fig. S9a manifested that 20% In-MOF/BiOF still kept relatively high adsorption and photocatalytic capacities after being reused for three times. The XRD pattern of the recycled photocatalyst was well consistent with the original one (Fig. S9b), further fortifying that the In-MOF/BiOF composites were stable and reusable.

The photodegradation of four typical PFASs (PFOA, PFOS, HFPO-TA and 6:2 Cl-PFESA) were further evaluated by 20% In-MOF/BiOF composite under the optimized conditions. The structural formula of PFOA, PFOS, HFPO-TA and 6:2 Cl-PFESA are listed in Table S4, and their degradation rates are illustrated in Fig. 4. 100% of PFOS, PFOA and 6:2 Cl-PFESA (15 mg/L) were removed within 90, 150 and 150 min of irradiation, respectively, while about 92% HFPO-TA (15 mg/L) was degraded during 180 min of irradiation. As shown in Fig. S10, in the control group without any photocatalyst, the photodegradation of the target compounds was negligible, verifying that the photocatalysts played an important role in their removal. The k_{obs} of PFOA, PFOS, HFPO-TA and 6:2 Cl-PFESA was 0.0141, 0.0861, 0.0126 and 0.0615 min^{-1} , following the order of PFOS > 6:2 Cl-PFESA > PFOA > HFPO-TA (Fig. S11). It is surprising that the 20% In-MOF/BiOF displayed excellent performance to PFOS degradation. Another study reported only 71% of PFOS was removed by advanced treatment processes like ultraviolet/advanced oxidation process (UV/AOP) or ozone combined with biological activated carbon filtration [55]. Recently, Sun et al. [56] reported it took 10 h to remove 60% of PFOS by a novel UV/Fe^{II}NTA photoreductive system. Zhu et al. [57] reported that Ga/TNTs@AC displayed high adsorption capacity to PFOS and could

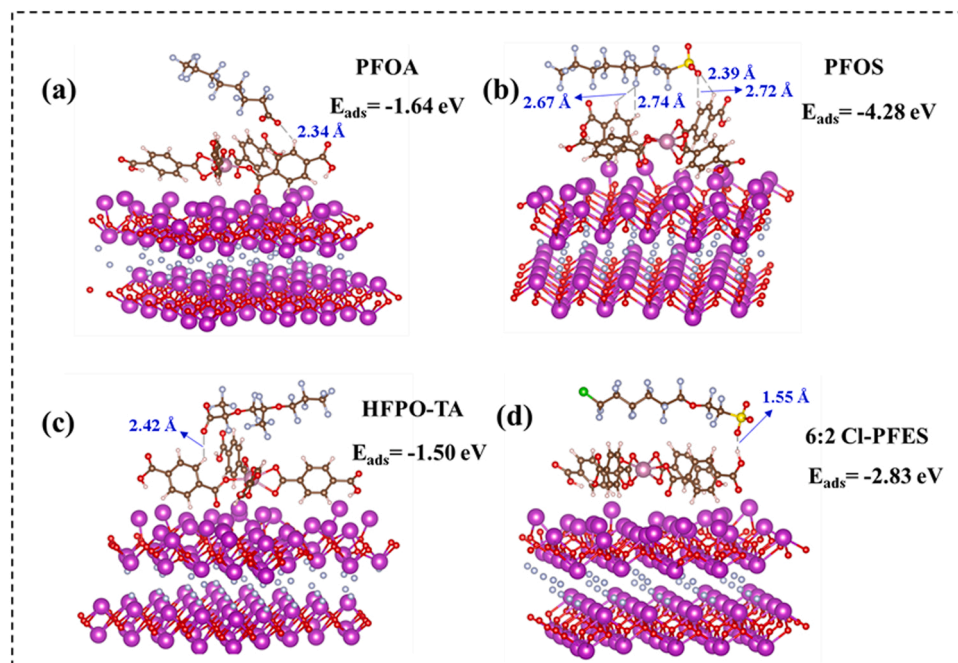


Fig. 5. DFT calculated adsorption energy of several pollutant molecules adsorbed on In-MOF/BiOF.

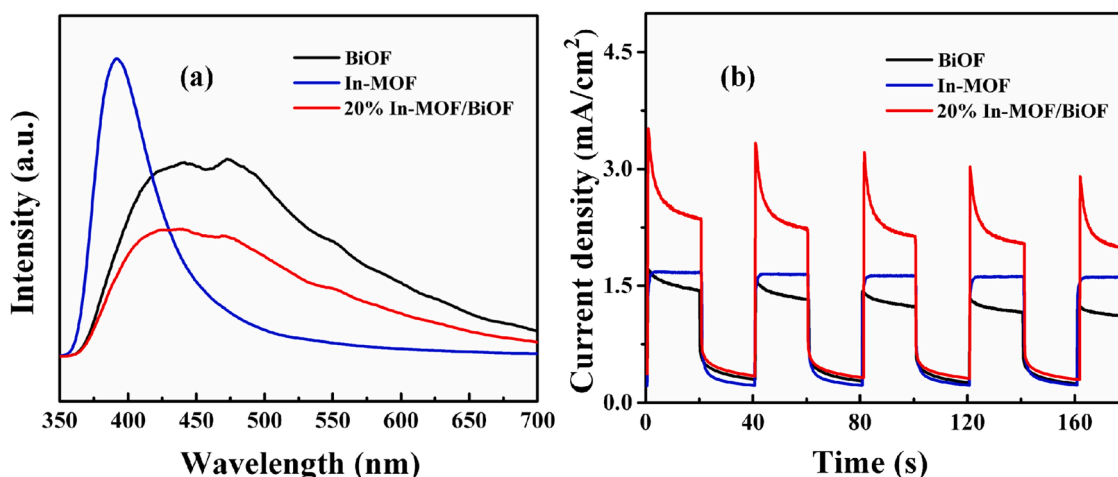


Fig. 6. PL spectra (a) and transient photocurrent response (b) of BiOF, In-MOF and 20% In-MOF/BiOF.

degrade 75.0% of pre-sorbed PFOS within 4 h UV irradiation. Comparatively, 20% In-MOF/BiOF exhibited superior performance in PFOS degradation.

The interaction between pollutant and photocatalyst surface plays an important role in photocatalytic reaction. In order to clearly explain the reasons for the different removal performances of the four target compounds, DFT analysis was carried out to investigate the interactions between them and In-MOF/BiOF at molecular level. The PFASs molecules could be spontaneously adsorbed on In-MOF/BiOF because of the negative adsorption energy, and they interacted with the surface atoms of In-MOF/BiOF via chemical bonds, as shown in Fig. 5. PFOA, HFPO-TA and 6:2 Cl-PFESA formed hydrogen bonds with a bond length of 2.34 Å, 2.42 Å and 1.55 Å, respectively. For PFOS, O and F interacted with the two H atoms on the adjacent benzene rings, respectively. Among the four compounds, PFOS had the strongest interaction with the photocatalyst with an adsorption energy (E_{ads}) of -4.28 eV, while that of PFOA, HFPO-TA and 6:2 Cl-PFESA was -1.64 , -1.50 and -2.83 eV, respectively. The negative value of E_{ads} represents the exothermic process. Generally, the larger the absolute value of E_{ads} is, the stronger the interaction between the catalyst surface and the adsorbate is, and the more stable the adsorption structure is. As shown in Fig. S12, there was a positive correlation between the reaction rate constant k_{obs} and the absolute value of E_{ads} of four PFASs ($R^2 = 0.961$), magnifying that the strong interaction between PFASs and In-MOF/BiOF was beneficial for the degradation of PFASs.

Further DFT calculation was conducted to show the difference charge density of the adsorbed species on In-MOF/BiOF (Fig. S13). The yellow and blue regions represent charge loss and charge accumulation, respectively. It is clear that the charge movement and rearrangement between In-MOF/BiOF and PFOS were more intensive and pronounced than other three compounds, suggesting that the PFOS molecule is distinctly activated due to adsorption on the surface of In-MOF/BiOF. Such activated state of PFOS is supposed to be conducive to the subsequent degradation reaction, which is in accordance with the highest degradation efficiency of PFOS.

3.3. The optical properties of the photocatalysts and active substances involved in the reaction systems

The optical properties of In-MOF, BiOF, 10%–40% In-MOF/BiOF were characterized by ultraviolet-visible diffusion reflectance spectra (Fig. S14a). The absorption edges of these materials were in the ultraviolet light region and ranged from 325 to 375 nm. 20% In-MOF/BiOF displayed stronger light absorption intensity, which contributed to its more outstanding degradation performance. The band gap energies (E_g) of In-MOF, BiOF and 20% In-MOF/BiOF were extrapolated based on the

Tauc equation of $(\alpha h\nu)^2 = C(h\nu - E_g)$, in which α , h , ν and C refer to the absorption coefficient, Planck constant, light frequency and constant value, respectively. The E_g of In-MOF, BiOF and 20% In-MOF/BiOF were about 3.78, 3.49 and 3.50 eV, respectively (Fig. S14b). According to the Mott-Scotty (M-S) test, the positive slopes of the M-S plots for both BiOF and In-MOF were characteristic of n-type semiconductors (Fig. S15).

The flat band potentials (E_{FB}) of BiOF and In-MOF were calculated to be -0.40 and -0.25 eV vs. Ag/AgCl. On the basis of $E_{\text{NHE}} = E_{\text{Ag/AgCl}} + 0.197$ eV, the E_{FB} of BiOF and In-MOF were converted to -0.203 and -0.053 eV vs. the normal H_2 electrode (NHE), respectively [58]. The bottom of the conduction band (CB) of an n-type semiconductor is usually 0.2 eV more negative than the E_{FB} , thus the CB positions (E_{CB}) of BiOF and In-MOF were estimated to be -0.40 and -0.25 eV [59]. Applying the empirical formula of $E_g = E_{\text{VB}} - E_{\text{CB}}$, the valence band positions (E_{VB}) of BiOF and In-MOF were 3.09 and 3.53 eV. The band structure parameters of BiOF and In-MOF are listed in Table S5.

As shown in Scheme S2, Fermi energy level of BiOF was more negative than that of In-MOF. Hence, the electrons moved from the Fermi level of BiOF to that of In-MOF until they reached a new equalization state, forming an internal electric field between BiOF and In-MOF. An n-n heterojunction formed in the contact region. Consequently, it is apparent that the e^- in CB of BiOF and In-MOF can reduce O_2 to form $\cdot\text{O}_2^-$ [60].

The predominant reactive oxidative species (ROS) of the photocatalytic degradation were studied to analyze the catalytic degradation mechanism. As shown in Fig. S16, ammonium oxalate (AO) [61], t-butanol (TBA) [62], p-benzoquinone (BQ) [33] and KBrO_3 [63] were used to capture h^+ , $\cdot\text{OH}$, $\cdot\text{O}_2^-$ and e^- in the reaction solutions, respectively. Both AO and BQ obviously depressed the degradation of PFOA, while TBA and KBrO_3 had an insignificant effect, implying that h^+ and $\cdot\text{O}_2^-$ were the main active species in the catalytic degradation of PFOA. To further confirm the radicals generated in the reaction system, EPR technology using DMPO as the radical spin-trapping probe was applied to detect $\cdot\text{O}_2^-$ radicals (Fig. S17). The characteristic peaks of $\cdot\text{O}_2^-$ were distinct in the spectra, and the signal intensities increased with the extension of time, demonstrating that $\cdot\text{O}_2^-$ was the main ROS which was responsible in the photocatalytic reaction.

In order to explore the transfer behavior and separation efficiency of photoexcited electron-hole pairs, the steady-state photoluminescence spectra (PL) and transient photocurrent response (PC) of BiOF, In-MOF and 20% In-MOF/BiOF were also conducted at room temperature. Fig. 6a shows a wide emission peak between 425 and 475 nm for BiOF and 20% In-MOF/BiOF with the excitation wavelength of 260 nm, while the PL spectra of In-MOF showed a characteristic peak at 387 nm with the excitation wavelength of 328 nm. Moreover, the fluorescence intensity increased in the order of 20% In-MOF/BiOF < BiOF < In-MOF,

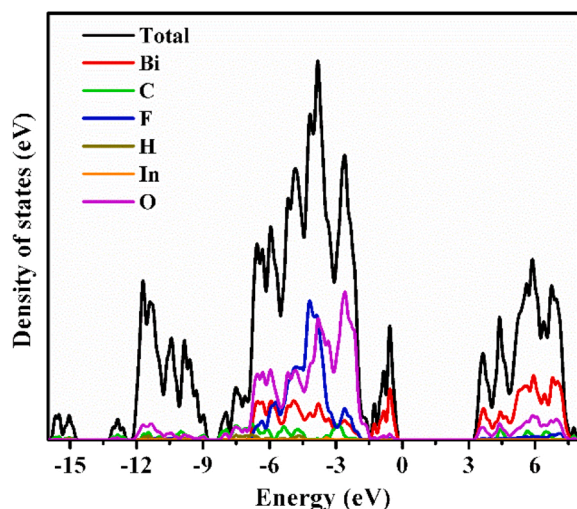


Fig. 7. Density of states (DOS) of In-MOF/BiOF composite. Black line denotes the total DOS, red line denotes the Bi 6p state, light green line denotes the C 2p state, blue line denotes the F 2p state, deep yellow line denotes the H 1s state, orange line denotes the In 5p state, and light purple line denotes the O 2p state.

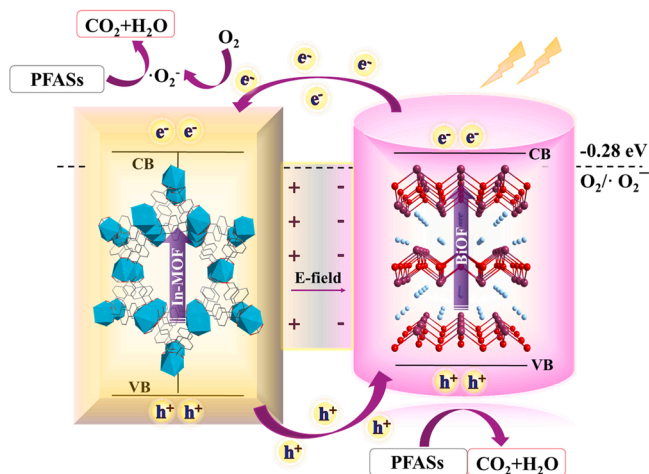
implying that the In-MOF/BiOF efficiently accelerated separation of the electron-hole pairs. The transient photocurrent response of the 20% In-MOF/BiOF was higher than those of pure BiOF and In-MOF, further demonstrating the doping of In-MOF greatly inhibited recombination of the photogenerated e^-h^+ pairs and achieved an effective interfacial charge separation (Fig. 6b).

3.4. Photocatalytic mechanisms on the basis of DFT calculations

In order to explore the band gap, the density of states (DOS) for all atoms in In-MOF, BiOF and In-MOF/BiOF composite were calculated by DFT method, and the optimized structures are shown in Fig. S18. As shown in Fig. S19a, In 5p and O 2p made the greatest contribution to the valence band edge in pure In-MOF, while the conduction band edge was contributed by C 2p, In 5p and O 2p states. Notably, the valence-band maximum (VBM) and the conduction-band minimum (CBM) were determined by In 5p and C 2p, respectively. Fig. S19b illustrates that O 2p and Bi 6p states in pure BiOF mainly contributed to the VBM and CBM, respectively. In In-MOF/BiOF (Fig. 7), the VBM was mainly determined by Bi 6p, while the CBM was mainly composed of Bi 6p, O 2p and C 2p. The calculated band gaps of In-MOF, BiOF and In-MOF/BiOF were 3.85, 3.27 and 3.32 eV, respectively, which were in good agreement with the experimental result, suggesting that the DFT calculation results are reliable.

In order to investigate the charge transfer and redistribution at the interface of In-MOF/BiOF composite, the 3D charge density difference was obtained using the following equation: $\Delta\rho = \rho_{\text{In-MOF/BiOF}} - \rho_{\text{BiOF}} - \rho_{\text{In-MOF}}$, in which $\rho_{\text{In-MOF/BiOF}}$, ρ_{BiOF} , $\rho_{\text{In-MOF}}$ represent the charge densities for In-MOF/BiOF, BiOF and In-MOF, respectively. In Fig. 8, yellow and cyan areas indicate charge accumulation and depletion respectively with isosurfaces set to be $0.0006 \text{ e}/\text{\AA}^3$. Fig. 8a illustrates that electrons mainly transfer from BiOF to In-MOF via the interface, leading to accumulation of net charges at In-MOF, resulting in the formation of a built-in electric field at the interface. Fig. 8b, c show the band charge density distribution in the composite, and the highest occupied energy band (HOEB) of In-MOF/BiOF is occupied by the orbital of Bi in BiOF bulk phase, while the lowest unoccupied energy band (LUEB) is occupied by that of Bi in the surface of BiOF and the C/O orbitals of In-MOF, which is in accordance with the result of DOS. The photogenerated electrons at HOEB could be easily excited to the LUEB as the In-MOF/BiOF was exposed to light. Thus, the photogenerated electrons of BiOF transfer to the In-MOF surface, leaving the photogenerated holes at HOEB. A built-in electric field was then generated with a direction from In-MOF to BiOF surface due to the net charge accumulation. As a result, the charge mobility was facilitated and separation of the e^-h^+ pairs was improved, which further explained the more effective photocatalysis performance of the In-MOF/BiOF composite.

On the basis of the above experimental data and calculated analyses, a possible mechanism for photocatalytic degradation of PFASs by In-MOF/BiOF composite is proposed in Scheme 1. Upon UV-light irradiation, photogenerated electrons and holes are formed at the surface of



Scheme 1. Schematic illustration of photocatalytic mechanism for In-MOF/BiOF composite under light irradiation.

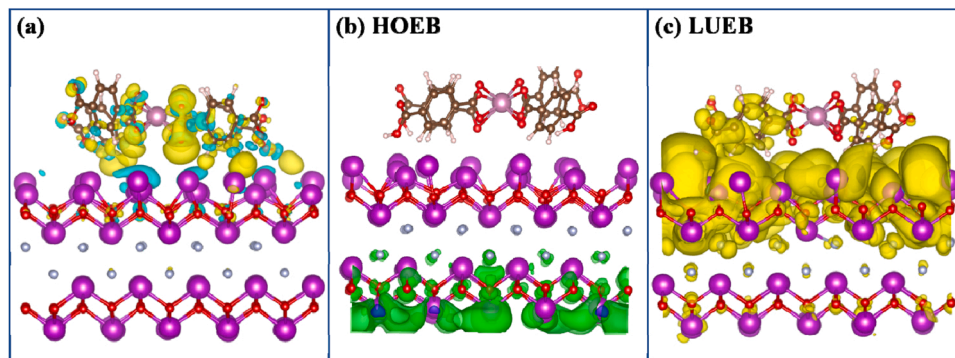


Fig. 8. (a) 3D charge density difference for the In-MOF/BiOF composite (yellow and cyan areas indicate charge accumulation and depletion with isosurfaces set to be $0.0006 \text{ e}/\text{\AA}^3$, respectively); (b) the energy band charge density distributions of HOEB, the green colors represent the charge density distribution with electron occupation; (c) the energy band charge density distributions of LUEB, the yellow colors represent the charge density distribution without electron occupation.

BiOF. The built-in electric field drives the photogenerated electrons of BiOF rapidly to transfer to the surface of In-MOF, and react with O_2 to form $\cdot O_2^-$. The photogenerated h^+ and $\cdot O_2^-$ as the main active species attack the target PFASs, and finally convert them into CO_2 and H_2O .

4. Conclusions

In this study, a series of novel In-MOF/BiOF heterojunctions in different doping ratios were successfully synthesized, characterized and evaluated for removal of several legacy and emerging PFASs. Introduction of 20% In-MOF in BiOF greatly enhanced its photocatalytic performance to degrade PFASs. It is particularly worth mentioning that the 20% In-MOF/BiOF composite not only exhibited high efficiency to degrade PFOA, but displayed superior performance to remove PFOS, which was much more difficult to degrade by other photocatalysts and advanced oxidative techniques. On the one hand, the DFT calculation results indicated that a built-in electric field was created at the interface between In-MOF and BiOF, which enhanced the efficient separation of photogenerated charge carriers. The results of radical trapping experiments and EPR spectroscopy measurement further confirmed that photogenerated h^+ and $\cdot O_2^-$ played critical roles in the photodegradation of the PFASs. On the other hand, In-MOF provides an active substrate for adsorption of PFASs, particularly for PFOS. The strong interactions between PFOS and the substrate help to activate the PFOS molecule, which favors its further degradation.

CRediT authorship contribution statement

Jingzhen Wang: Conceptualization, Investigation, Resources, Data curation, Writing – original draft. **Chun-Shuai Cao:** Conceptualization, Investigation, Resources, Data curation, Writing – original draft. **Jingwen Wang:** Investigation, Resources. **Yinqing Zhang:** Supervision, Writing – review & editing. **Lingyan Zhu:** Conceptualization, Supervision, Writing – review & editing, Supervision, Project administration, Funding acquisition.

Declaration of Competing Interest

The authors declare that they have no known competing financial interests or personal relationships that could have appeared to influence the work reported in this paper.

Acknowledgments

The authors gratefully acknowledge financial support from National Natural Science Foundation of China (NSFC 41991313, 22106074, and 22111530176), the National Key Research and Development Program of China (2018YFC1801003), Tianjin Natural Science Foundation (20JCQNJC01840) and the 111 Program of Ministry of Education of China (T2017002). We gratefully acknowledge the support from Prof. Weichao Wang (Nankai University) in theoretical calculations.

Appendix A. Supplementary material

Supplementary data associated with this article can be found in the online version at [doi:10.1016/j.apcatb.2021.121013](https://doi.org/10.1016/j.apcatb.2021.121013).

References

- [1] L. Ahrens, J.P. Benskin, I.T. Cousins, M. Crimi, C.P. Higgins, Themed issues on per- and polyfluoroalkyl substances, *Environ. Sci. Process. Impacts* 21 (2019) 1797–1802.
- [2] P. Casal, B. González-Gaya, Y. Zhang, A.J.F. Reardon, J.W. Martin, B. Jiménez, J. Dachs, Accumulation of perfluoroalkylated substances in oceanic plankton, *Environ. Sci. Technol.* 51 (2017) 2766–2775.
- [3] M. Sun, E. Arevalo, M. Strynar, A. Lindstrom, M. Richardson, B. Kearns, A. Pickett, C. Smith, D.R.U. Knappe, Legacy and emerging perfluoroalkyl substances are

- important drinking water contaminants in the Cape Fear River watershed of North Carolina, *Environ. Sci. Technol. Lett.* 3 (2016) 415–419.
- [4] C. Lau, K. Anitole, C. Hodes, D. Lai, A. Pfahles-Hutchens, J. Seed, Perfluoroalkyl acids: a review of monitoring and toxicological findings, *Toxicol. Sci.* 99 (2007) 366–394.
- [5] Z.Y. Wang, I.T. Cousins, M. Scheringer, K. Hungerbuehler, Hazard assessment of fluorinated alternatives to long-chain perfluoroalkyl acids (PFAAs) and their precursors: status quo, ongoing challenges and possible solutions, *Environ. Int.* 75 (2015) 172–179.
- [6] I.T. Cousins, G. Goldenman, D. Herzke, R. Lohmann, M. Miller, C.A. Ng, S. Patton, M. Scheringer, X. Trier, L. Vierke, Z. Wang, J.C. DeWitt, The concept of essential use for determining when uses of PFAAs can be phased out, *Environ. Sci. Process. Impacts* 21 (2019) 1803–1815.
- [7] T. Wang, Y.W. Wang, C.Y. Liao, Y.Q. Cai, G.B. Jiang, Perspectives on the inclusion of perfluorooctane sulfonate into the Stockholm convention on persistent organic pollutants, *Environ. Sci. Technol.* 43 (2009) 5171–5175.
- [8] S. Wang, J. Huang, Y. Yang, Y. Hui, Y. Ge, T. Larssen, G. Yu, S. Deng, B. Wang, C. Harman, First report of a Chinese PFOS alternative overlooked for 30 years: its toxicity, persistence, and presence in the environment, *Environ. Sci. Technol.* 47 (2013) 10163–10170.
- [9] Z. Wang, I.T. Cousins, M. Scheringer, K. Hungerbuehler, Fluorinated alternatives to long-chain perfluoroalkyl carboxylic acids (PFCAs), perfluoroalkane sulfonic acids (PFASs) and their potential precursors, *Environ. Int.* 60 (2013) 242–248.
- [10] N. Sheng, Y. Guo, Y. Sun, J. Dai, Hepatotoxic effects of hexafluoropropylene oxide trimer acid (HFPO-TA), a novel perfluorooctanoic acid (PFOA) alternative, on mice, *Environ. Sci. Technol.* 52 (2018) 8005–8015.
- [11] N. Sheng, R. Cui, J. Wang, Y. Guo, J. Wang, J. Dai, Cytotoxicity of novel fluorinated alternatives to long-chain perfluoroalkyl substances to human liver cell line and their binding capacity to human liver fatty acid binding protein, *Arch. Toxicol.* 92 (2017) 359–369.
- [12] N. Sheng, X. Zhou, F. Zheng, Y. Pan, X. Guo, Y. Guo, Y. Sun, J. Dai, Comparative hepatotoxicity of 6:2 fluorotelomer carboxylic acid and 6:2 fluorotelomer sulfonic acid, two fluorinated alternatives to long-chain perfluoroalkyl acids, on adult male mice, *Arch. Toxicol.* 91 (2017) 2909–2919.
- [13] X. Feng, M. Ye, Y. Li, J. Zhou, B. Sun, Y. Zhu, L. Zhu, Potential sources and sediment-pore water partitioning behaviors of emerging per/polyfluoroalkyl substances in the South Yellow Sea, *J. Hazard. Mater.* 389 (2020), 122124.
- [14] Y. Li, X. Feng, J. Zhou, L. Zhu, Occurrence and source apportionment of novel and legacy poly/perfluoroalkyl substances in Hai River basin in China using receptor models and isomeric fingerprints, *Water Res.* 168 (2020), 115145.
- [15] E. Shang, Y. Li, J. Niu, S. Li, G. Zhang, X. Wang, Photocatalytic degradation of perfluorooctanoic acid over Pb-BiFeO₃/rGO catalyst: kinetics and mechanism, *Chemosphere* 211 (2018) 34–43.
- [16] J.Z. Wang, C.S. Cao, Y.Y. Wang, Y.N. Wang, B.B. Sun, L.Y. Zhu, In situ preparation of p-n BiOI@Bi₅O₇I heterojunction for enhanced PFOA photocatalytic degradation under simulated solar light irradiation, *Chem. Eng. J.* 391 (2020), 123530.
- [17] J.Z. Wang, Y.N. Wang, C.S. Cao, Y. Zhang, Y.Q. Zhang, L.Y. Zhu, Decomposition of highly persistent perfluorooctanoic acid by hollow Bi/BiOI_{1-x}F_x: synergistic effects of surface plasmon resonance and modified band structures, *J. Hazard. Mater.* 402 (2021), 123459.
- [18] Z. Li, P. Zhang, T. Shao, X. Li, In₂O₃ nanoporous nanosphere: a highly efficient photocatalyst for decomposition of perfluorooctanoic acid, *Appl. Catal. B Environ.* 125 (2012) 350–357.
- [19] J. Zhong, Y. Zhao, L. Ding, H. Ji, W. Ma, C. Chen, J. Zhao, Opposite photocatalytic oxidation behaviors of BiOI and TiO₂: direct hole transfer vs. indirect-OH oxidation, *Appl. Catal. B Environ.* 241 (2018) 514–520.
- [20] S. He, C. Yan, X.-Z. Chen, Z. Wang, T. Ouyang, M.-L. Guo, Z.-Q. Liu, Construction of core-shell heterojunction regulating α -Fe₂O₃ layer on CeO₂ nanotube arrays enables highly efficient Z-scheme photoelectrocatalysis, *Appl. Catal. B Environ.* 276 (2020), 119138.
- [21] D. Liu, W. Cai, Y. Wang, Y. Zhu, Constructing a novel Bi₂SiO₅/BiPO₄ heterostructure with extended light response range and enhanced photocatalytic performance, *Appl. Catal. B Environ.* 236 (2018) 205–211.
- [22] T. Wang, C. Nie, Z. Ao, S. Wang, T. An, Recent progress in g-C₃N₄ quantum dots: synthesis, properties and applications in photocatalytic degradation of organic pollutants, *J. Mater. Chem. A* 8 (2020) 485–502.
- [23] M. Chu, K. Hu, J. Wang, Y. Liu, S. Ali, C. Qin, L. Jing, Synthesis of g-C₃N₄-based photocatalysts with recyclable feature for efficient 2,4-dichlorophenol degradation and mechanisms, *Appl. Catal. B Environ.* 243 (2019) 57–65.
- [24] D.J. Martin, N. Umezawa, X. Chen, J.H. Ye, J.W. Tang, Facet engineered Ag₃PO₄ for efficient water photooxidation, *Energy Environ. Sci.* 6 (2013) 3380–3386.
- [25] J. Zwara, E. Grabowska, T. Klimczuk, W. Lisowski, A. Zaleska-Medynska, Shape-dependent enhanced photocatalytic effect under visible light of Ag₃PO₄ particles, *J. Photochem. Photobiol. A Chem.* 367 (2018) 240–252.
- [26] L. Ye, K.H. Chu, B. Wang, D. Wu, H. Xie, G. Huang, H.Y. Yip, P.K. Wong, Noble metal loading reverses temperature dependent photocatalytic hydrogen generation in methanol-water solutions, *Chem. Commun.* 52 (2016) 11657–11660.
- [27] A.B. Trench, T.R. Machado, A.F. Gouveia, M. Assis, L.G. da Trindade, C. Santos, A. Perrin, C. Perrin, M. Oliva, J. Andrés, E. Longo, Connecting structural, optical, and electronic properties and photocatalytic activity of Ag₃PO₄: Mo complemented by DFT calculations, *Appl. Catal. B Environ.* 238 (2018) 198–211.
- [28] J. Tian, Z. Zhao, A. Kumar, R.I. Boughton, H. Liu, Recent progress in design, synthesis, and applications of one-dimensional TiO₂ nanostructured surface heterostructures: a review, *Chem. Soc. Rev.* 43 (2014) 6920–6937.

- [29] Y. Lin, C. Yang, S. Wu, X. Li, Y. Chen, W.L. Yang, Construction of built-in electric field within silver phosphate photocatalyst for enhanced removal of recalcitrant organic pollutants, *Adv. Funct. Mater.* 30 (2020), 2002918.
- [30] P. Cui, D. Wei, J. Ji, H. Huang, E. Jia, S. Dou, T. Wang, W. Wang, M. Li, Planar p-n homojunction perovskite solar cells with efficiency exceeding 21.3%, *Nat. Energy* 4 (2019) 150–159.
- [31] L. Ye, J. Liu, Z. Jiang, T. Peng, L. Zan, Facets coupling of BiOBr-g-C₃N₄ composite photocatalyst for enhanced visible-light-driven photocatalytic activity, *Appl. Catal. B Environ.* 142–143 (2013) 1–7.
- [32] S. Chen, R. Yan, X. Zhang, K. Hu, Z. Li, M. Humayun, Y. Qu, L. Jing, Photogenerated electron modulation to dominantly induce efficient 2,4-dichlorophenol degradation on BiOBr nanoplates with different phosphate modification, *Appl. Catal. B Environ.* 209 (2017) 320–328.
- [33] S. Cui, G. Shan, L. Zhu, Solvothermal synthesis of I-deficient BiOI thin film with distinct photocatalytic activity and durability under simulated sunlight, *Appl. Catal. B Environ.* 219 (2017) 249–258.
- [34] S. Vadivel, V.P. Kamalakannan, N.P. Kavitha, T. Santhoshini Priya, N. Balasubramanian, Development of novel Ag modified BiOF squares/g-C₃N₄ composite for photocatalytic applications, *Mater. Sci. Semicond. Proc.* 41 (2016) 59–66.
- [35] J. Wang, C. Cao, Y. Zhang, Y. Zhang, L. Zhu, Underneath mechanisms into the super effective degradation of PFOA by BiOF nanosheets with tunable oxygen vacancies on exposed (101) facets, *Appl. Catal. Environ.* 286 (2021), 119911.
- [36] L. Valenzano, B. Civalieri, S. Chavan, S. Bordiga, M.H. Nilsen, S. Jakobsen, K. P. Lillerud, C. Lamberti, Disclosing the complex structure of UiO-66 metal organic framework: a synergic combination of experiment and theory, *Chem. Mater.* 23 (2011) 1700–1718.
- [37] F. Leng, H. Liu, M. Ding, Q.-P. Lin, H.-L. Jiang, Boosting photocatalytic hydrogen production of porphyrinic MOFs: the metal location in metalloporphyrin matters, *ACS Catal.* 8 (2018) 4583–4590.
- [38] I.F. Teixeira, E.C.M. Barbosa, S.C.E. Tsang, P.H.C. Camargo, Carbon nitrides and metal nanoparticles: from controlled synthesis to design principles for improved photocatalysis, *Chem. Soc. Rev.* 47 (2018) 7783–7817.
- [39] C.-S. Cao, J. Wang, X. Yu, Y. Zhang, L. Zhu, Photodegradation of seven bisphenol analogues by Bi₅O₇I/UiO-67 heterojunction: relationship between the chemical structures and removal efficiency, *Appl. Catal. B Environ.* 277 (2020), 119222.
- [40] H. Yu, S. Chen, X. Fan, X. Quan, H. Zhao, X. Li, Y. Zhang, A structured macroporous silicon/graphene heterojunction for efficient photoconversion, *Angew. Chem. Int. Ed.* 49 (2010) 5106–5109.
- [41] Y. Gong, B. Yang, H. Zhang, X. Zhao, A g-C₃N₄/MIL-101(Fe) heterostructure composite for highly efficient BPA degradation with persulfate under visible light irradiation, *J. Mater. Chem. A* 6 (2018) 23703–23711.
- [42] L. Shen, M. Luo, Y. Liu, R. Liang, F. Jing, L. Wu, Noble-metal-free MoS₂ co-catalyst decorated UiO-66/CdS hybrids for efficient photocatalytic H₂ production, *Appl. Catal. B Environ.* 166–167 (2015) 445–453.
- [43] W. Ji, H. Hu, W. Zhang, H. Huang, X. He, X. Han, F. Zhao, Y. Liu, Z. Kang, Indium (III)-dicarboxylic microporous frameworks with high adsorption selectivity for CO₂ over N₂, *Dalton Trans.* 42 (2013) 10690–10693.
- [44] G. Kresse, J. Furthmüller, Efficient iterative schemes for ab initio total-energy calculations using a plane-wave basis set, *Phys. Rev. B* 54 (1996) 11169–11186.
- [45] G. Kresse, J. Furthmüller, Efficiency of ab-initio total energy calculations for metals and semiconductors using a plane-wave basis set, *Comput. Mater. Sci.* 6 (1996) 15–50.
- [46] J.P. Perdew, K. Burke, M. Ernzerhof, Generalized gradient approximation made simple, *Phys. Rev. Lett.* 77 (1996) 3865–3868.
- [47] J.P. Perdew, M. Ernzerhof, K. Burke, Rationale for mixing exact exchange with density functional approximations, *J. Chem. Phys.* 105 (1996) 9982–9985.
- [48] S. Grimme, Semiempirical GGA-type density functional constructed with a long-range dispersion correction, *J. Comput. Chem.* 27 (2006) 1787–1799.
- [49] Y. Su, Z. Zhang, H. Liu, Y. Wang, Cd_{0.2}Zn_{0.8}S@UiO-66-NH₂ nanocomposites as efficient and stable visible-light-driven photocatalyst for H₂ evolution and CO₂ reduction, *Appl. Catal. B Environ.* 200 (2017) 448–457.
- [50] C. Tian, J. Zhao, X. Ou, J. Wan, Y. Cai, Z. Lin, Z. Dang, B. Xing, Enhanced adsorption of p-arsanilic acid from water by amine-modified UiO-67 as examined using extended X-ray absorption fine structure, X-ray photoelectron spectroscopy, and density functional theory calculations, *Environ. Sci. Technol.* 52 (2018) 3466–3475.
- [51] Z. Dong, J. Pan, B. Wang, Z. Jiang, C. Zhao, J. Wang, C. Song, Y. Zheng, C. Cui, C. Li, The p-n-type Bi₅O₇I-modified porous g-C₃N₄ nano-heterojunction for enhanced visible light photocatalysis, *J. Alloy. Compd.* 747 (2018) 788–795.
- [52] K. Wang, Y. Li, G. Zhang, J. Li, X. Wu, 0D Bi nanodots/2D Bi₃NbO₇ nanosheets heterojunctions for efficient visible light photocatalytic degradation of antibiotics: enhanced molecular oxygen activation and mechanism insight, *Appl. Catal. B Environ.* 240 (2019) 39–49.
- [53] C. Gan, C. Xu, H. Wang, N. Zhang, J. Zhang, Y. Fang, Facile synthesis of rGO@In₂S₃@UiO-66 ternary composite with enhanced visible-light photodegradation activity for methyl orange, *J. Photochem. Photobiol. A* 384 (2019), 112025.
- [54] C. Yang, S. Wu, J. Cheng, Y. Chen, Indium-based metal-organic framework/graphite oxide composite as an efficient adsorbent in the adsorption of rhodamine B from aqueous solution, *J. Alloy. Compd.* 687 (2016) 804–812.
- [55] C.M. Glover, O. Quinones, E.R.V. Dickenson, Removal of perfluoroalkyl and polyfluoroalkyl substances in potable reuse systems, *Water Res.* 144 (2018) 454–461.
- [56] Z.Y. Sun, C.J. Zhang, J.C. Jiang, J. Wen, Q. Zhou, M.R. Hoffmann, UV/Fe^{II}-NTA as a novel 56photoreductive system for the degradation of perfluorooctane sulfonate (PFOS) via a photoinduced intramolecular electron transfer mechanism, *Chem. Eng. J.* 427 (2022), 130923.
- [57] Y. Zhu, T. Xu, D. Zhao, F. Li, W. Liu, B. Wang, B. An, Adsorption and solid-phase photocatalytic degradation of perfluorooctane sulfonate in water using gallium-doped carbon-modified titanate nanotubes, *Chem. Eng. J.* 421 (2021), 129676.
- [58] Q. Liang, S. Cui, C. Liu, S. Xu, C. Yao, Z. Li, Self-assembly of triptycene-based polymer on cadmium sulfide nanorod to construct core-shell nanostructure for efficient visible-light-driven photocatalytic H₂ evolution, *Chem. Eng. J.* 364 (2019) 102–110.
- [59] Y. Xiao, Y. Qi, X. Wang, X. Wang, F. Zhang, C. Li, Visible-light-responsive 2D cadmium-organic framework single crystals with dual functions of water reduction and oxidation, *Adv. Mater.* 30 (2018) 1803401–1803408.
- [60] F. Xing, C. Cheng, J. Zhang, Q. Liu, C. Chen, C. Huang, Tunable charge transfer efficiency in H₃MoO₃@ZnIn₂S₄ hierarchical direct Z-scheme heterojunction toward efficient visible-light-driven hydrogen evolution, *Appl. Catal. B Environ.* 285 (2021), 119818.
- [61] R. Yuan, C. Yue, J. Qiu, F. Liu, A. Li, Highly efficient sunlight-driven reduction of Cr (VI) by TiO₂@NH₂-MIL-88B (Fe) heterostructures under neutral conditions, *Appl. Catal. B Environ.* 251 (2019) 229–239.
- [62] B. Darsinou, Z. Frontistis, M. Antonopoulou, I. Konstantinou, D. Mantzavinos, Sonoactivated persulfate oxidation of bisphenol A: kinetics, pathways and the controversial role of temperature, *Chem. Eng. J.* 280 (2015) 623–633.
- [63] J.-J. Du, Y.-P. Yuan, J.-X. Sun, F.-M. Peng, X. Jiang, L.-G. Qiu, A.-J. Xie, Y.-H. Shen, J.-F. Zhu, New photocatalysts based on MIL-53 metal-organic frameworks for the decolorization of methylene blue dye, *J. Hazard. Mater.* 190 (2011) 945–951.